Journal of Computational Physics **165,** 22–44 (2000)
doi:10.1006/jcph.2000.6594, available online at http://www.idealibrary.com on IDEAL®

Developing High-Order Weighted Compact Nonlinear Schemes

Xiaogang Deng and Hanxin Zhang

Computational Aerodynamic Institute of CARDC, P.O. Box 211, Mianyang,
Sichuan 621000, People's Republic of China

Received November 1, 1999; revised May 17, 2000; published online November 3, 2000

The weighted technique is introduced in the compact high-order nonlinear schemes (CNS) and three fourth- and fifth-order weighted compact nonlinear schemes (WCNS) are developed in this paper. By Fourier analysis, the dissipative and dispersive features of WCNS are discussed. In view of the modified wave number, the WCNS are equivalent to fifth-order upwind biased explicit schemes in smooth regions and the interpolations at cell-edges dominate the properties of WCNS. Both flux difference splitting and flux vector splitting methods can be applied in WCNS, though they are finite difference schemes. Boundary and near boundary schemes are developed and the asymptotic stability of WCNS is analyzed. Several numerical results are given which show the good performances of WCNS for discontinuity capture high accuracy for boundary layer calculation, and good convergent rate. We also compare WCNS with MUSCL scheme and spectral solutions. WCNS are more accurate than MUSCL, as expected, especially for heat transfer calculations. © 2000 Academic Press

Key Words: compact schemes; nonlinear schemes; finite difference schemes; Euler equations; Navier–Stokes equations.

1. INTRODUCTION

In the 1990s, compact schemes for the direct numerical simulation of turbulence and aeroacoustic calculations have received much attention. Lele [1] analyzed a series of compact schemes and derived compact schemes with spectral resolutions. Wilson *et al.* [2] proposed high-order compact schemes and discussed then application to incompressible Navier–Stokes equation calculations. Leslie and Purser [3] derived cell-centered fourth-order compact schemes and solved a regional forecast model. Garanzha and Konshin [4] developed numerical algorithms for viscous incompressible fluid flows based on cell-centered compact schemes. Gaitonde and Shang [5] and Kobayashi [6] proposed and analyzed finite-volume compact schemes and so forth. Despite their differences these schemes are all linear ones. For nonlinear compact schemes, the research work is less compared to linear schemes. Cockburn and Shu [7] proposed third- and fourth-order compact nonlinear schemes based on TVD and TVB concepts, but the solutions near shock waves oscillate obviously for the fourth-order schemes.

In this paper, we continue the development of compact high-order nonlinear schemes (CNS). Third- and fourth-order compact nonlinear schemes (CNS3, CNS4) were derived in our previous work [8, 9]. These schemes achieve high-order accuracy by cell-centered fourth-order compact schemes and compact high-order interpolations at cell-edges are designed. Two propositions, which guarantee the uniform high order of the interpolations, were proved. The numerical solutions for the Euler equations showed that CNS3 and CNS4 can capture discontinuities robustly. One advantage of these schemes is that primitive variables, conservative variables, and flux themselves can be used for the calculation of numerical flux at the cell-edges though they are finite difference formulations. The efficiency of CNS3 and CNS4, however, is relatively low due to the three tridiagonal inversions that are needed for the calculation of the derivative, and the contact discontinuity is somewhat smeared. Furthermore, in smooth regions only parts of the useful information are used because the compact adaptive interpolations also play a role in these regions. Recently a weighted technique was introduced in ENO schemes by Liu *et al.* [12] and improved by Jiang and Shu [13], such that weighted ENO schemes were developed. The analytic work shows that WENO schemes are more efficient and more accurate in a smooth region than ENO schemes [13]. Moreover, no logical statements, which perform poorly on vector supercomputers, are required in WENO schemes. However, in view of the one-dimensional blast wave calculations, the WENO schemes of Jiang and Shu did not resolve well the contact discontinuity resulting from wave interactions, though Yang's artificial compression method was used in their calculations. Furthermore, in [13] only the interior schemes are discussed. It is not known how the boundary and near boundary conditions have been applied for WENO, which is very important for high-order scheme applications.

The objective of the present paper is to develop high-order CNS based on the weighted technique, such that weighted compact nonlinear schemes (WCNS) are obtained, which need only one tridiagonal inversion for derivative calculations and are fourth- or fifth-order accurate in smooth regions. By Fourier analysis, the dispersive and dissipative features of WCNS are discussed. Boundary and near boundary schemes are derived and asymptotic stability is analyzed on both uniform and stretching grids. For contact discontinuity sharpening, the method of Huynh [15] is adopted. In Section 3, the WCNS are applied to Euler and Navier–Stokes equations and several numerical results are obtained which show the good performances of WCNS, especially the good convergence rate and high accuracy for the boundary layer simulations.

2. NUMERICAL METHODOLOGY

In this paper we consider numerical approximations to solutions of three-dimensional Navier–Stokes equations in general coordinates,

$$\frac{\partial U}{\partial t} + \frac{\partial E_l}{\partial \xi_l} = \frac{\partial E_{vl}}{\partial \xi_l}, \tag{1}$$

where the vectors U, E_l, and E_{vl} are dependent variables, convective flux, and viscous flux in the lth spatial coordinate, respectively ($l = 1, 2, 3$), i.e.,

$$U = J\begin{pmatrix}\rho\\ \rho u_1\\ \rho u_2\\ \rho u_3\\ e\end{pmatrix}, \quad E_l = J\begin{pmatrix}\rho V_l\\ \rho V_l u_1 + \xi_{lx} p\\ \rho V_l u_2 + \xi_{ly} p\\ \rho V_l u_3 + \xi_{lz} p\\ (e+p)V_l\end{pmatrix}, \quad E_{\mathrm{v}l} = J\begin{pmatrix}0\\ \xi_{lx}\tau_{11} + \xi_{ly}\tau_{12} + \xi_{lz}\tau_{13}\\ \xi_{lx}\tau_{21} + \xi_{ly}\tau_{22} + \xi_{lz}\tau_{23}\\ \xi_{lx}\tau_{31} + \xi_{ly}\tau_{32} + \xi_{lz}\tau_{33}\\ \xi_{lx}\beta_1 + \xi_{ly}\beta_2 + \xi_{lz}\beta_3\end{pmatrix},$$

with

$$\begin{aligned}
p &= \frac{1}{\gamma M_\infty^2}\rho T,\\
e &= \frac{p}{(\gamma-1)} + \frac{\rho}{2}u_m u_m,\\
\tau_{ij} &= \frac{\mu}{\mathrm{Re}}\left(\frac{\partial u_i}{\partial x_j} + \frac{\partial u_j}{\partial x_i} - \frac{2}{3}\delta_{ij}\frac{\partial u_m}{\partial x_m}\right),\\
\beta_i &= \tau_{im}u_m + \frac{\mu}{(\gamma-1)\,\mathrm{Re}\, M_\infty^2 \mathrm{Pr}}\frac{\partial T}{\partial x_i},
\end{aligned}$$

where γ is the ratio of specific heats and the viscous coefficient μ can be calculated by Sutherland's law. The nondimensional variables are defined as $\rho = \rho^*/\rho_\infty^*$, $u_l = u_l^*/u_\infty^*$, $T = T^*/T_\infty^*$, and $p = p^*/p_\infty^* u_\infty^{*2}$, respectively, and $M_\infty = u_\infty^*/\sqrt{\gamma R T_\infty^*}$, $\mathrm{Re} = \rho_\infty^* u_\infty^* r^*/\mu_\infty^*$ and $\mathrm{Pr} = \mu_\infty^* C_p/\kappa_\infty^*$ are the Mach number, Reynolds number, and Prandtl number, and r^* is the characteristic length. J is the Jacobian of grid transformation, ξ_{lt}, ξ_{lx}, ξ_{ly}, and ξ_{lz} are grid derivatives, and $V_l = \xi_{lt} + u\xi_{lx} + v\xi_{ly} + w\xi_{lz}$.

The Cell-centered Compact Schemes

The governing Eqs. (1) can be discretized line by line in the computational space (ξ_1, ξ_2, ξ_3). Therefore, in this section, we only consider one-dimensional convective flux discretization for simplicity. Let $U_j = U(x_j, t)$, let $x_j = jh$, and denote a numerical approximation to the solution of the equation

$$\frac{\partial U}{\partial t} + \frac{\partial E}{\partial x} = 0. \tag{2}$$

At every node x_j, we discrete Eq. (2) by the semi-discrete finite difference scheme

$$\left(\frac{\partial U}{\partial t}\right)_j = -E_j', \tag{3}$$

where E_j' is the approximation to the spatial derivative. As discussed in Refs. [1, 8, 11], the cell-centered finite difference compact schemes (CCS) are used to calculate E_j' which have the form

$$\kappa E_{j-1}' + E_j' + \kappa E_{j+1}' = \frac{a}{h}\left(\tilde{E}_{j+1/2} - \tilde{E}_{j-1/2}\right) + \frac{b}{h}\left(\tilde{E}_{j+3/2} - \tilde{E}_{j-3/2}\right), \tag{4}$$

with the parameters

$$a = \frac{3}{8}(3 - 2\kappa), \quad b = \frac{1}{24}(22\kappa - 1),$$

where $\tilde{E}_{j\pm1/2} = E(\tilde{U}_{j\pm1/2})$ is the numerical flux at the cell-edges. By the Taylor series expansion of (4), we may get

$$E'_j = \left(\frac{\partial E}{\partial x}\right)_j + \frac{9 - 62\kappa}{1920} h^4 E_j^{(5)} + O(h^r) + O(h^6). \tag{5}$$

The truncation term $O(h^r)$ comes from the interpolations of $\tilde{U}$. If $\tilde{U}_{j\pm1/2}$ approximates $U_{j\pm1/2}$ to the fifth-order ($r = 5$), which is the case in the present paper, the schemes are fourth- or fifth-order accurate depending on the parameter κ. In this paper, the following three cases are discussed:

(1) $\kappa = \frac{1}{22}$ (WCNS-4),

$$\kappa E'_{j-1} + E'_j + \kappa E'_{j+1} = \frac{a}{h}\left(\tilde{E}_{j+1/2} - \tilde{E}_{j-1/2}\right). \tag{6}$$

This is the most compact fourth-order scheme and was used in CNS [8, 9]. Leslie and Purse [3] also derived this scheme.

(2) $\kappa = \frac{9}{62}$ (WCNS-5),

$$\kappa E'_{j-1} + E'_j + \kappa E'_{j+1} = \frac{a}{h}\left(\tilde{E}_{j+1/2} - \tilde{E}_{j-1/2}\right) + \frac{b}{h}\left(\tilde{E}_{j+3/2} - \tilde{E}_{j-3/2}\right). \tag{7}$$

In this case the scheme is fifth-order accurate. If $\tilde{E} = E$, i.e., without interpolation errors of U at cell edges, it is sixth-order.

(3) $\kappa = 0$ (WCNS-E-4),

$$E'_j = \frac{a}{h}\left(\tilde{E}_{j+1/2} - \tilde{E}_{j-1/2}\right) + \frac{b}{h}\left(\tilde{E}_{j+3/2} - \tilde{E}_{j-3/2}\right). \tag{8}$$

This is an explicit scheme and more efficient than WCNS-4 and WCNS-5, because non-tridiagonal inversion is required.

Cell-centered compact schemes have the advantage over unstaggered schemes that their dispersive errors are considerably lower [1]. This feature can be seen clearly from Fig. 1, which plots the modified wave numbers for CCS-4, CCS-6, and CCS-E-4, which correspond to WCNS-4, WCNS-5, and WCNS-E-4 as $\tilde{E} = E$, respectively. To compare, the cell-centered with the unstaggered compact schemes, the Pàde schemes (fourth-order) and sixth-order compact scheme (CS-6) of Lele [1] are also shown in this figure.

It should be pointed out if $\tilde{U}$ are only rth order accurate approximations of U at cell-edges, i.e., $\tilde{E} = E + O(h^r)$, the dispersive and dissipative properties of CCS are dominated by $\tilde{U}$. Thus, it is important to get high-order interpolation of $\tilde{U}$ at cell-edges. We will further discuss this feature in the next section.

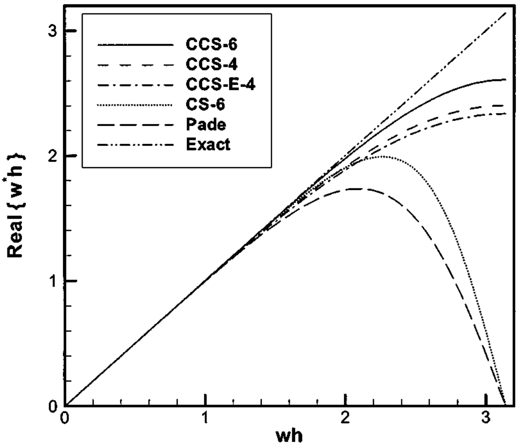

FIG. 1. The modified wave numbers for various compact schemes.

Weighted Interpolations at Cell Edges

In [8, 9], the third- and fourth-order compact adaptive interpolations at cell-edges were derived and compact nonlinear schemes (CNS-3, CNS-4) were obtained. The main idea in designing these interpolations is to prevent them from crossing the discontinuities, so that uniform high order is achieved even for discontinuous data. Though CNS worked well, two problems arose. First CNS contain three tridiagonal inversions that made CNS less efficient than explicit schemes. Second CNS was involved in three grid stencils for each grid point derivative calculation, but only one stencil information was finally selected, which resulted in a waste of information in smooth regions. We used the weighted technique of Jiang and Shu [13] to solve these problems. The idea is that each of the three stencils is assigned a weight which determines the contribution of the stencil to the final approximations of the cell-edge value. The weights are designed in such a way that in a smooth region they approach the optimal weights to achieve fifth-order accuracy and require nontridiagonal inversion. In regions near discontinuities, the stencils which contain the discontinuities are assigned nearly zero weights, so that third-order interpolations are achieved in these regions. Thus, the weighted interpolations are also prevented from crossing discontinuities. This technique completely removes the logical statements that appeared in CNS. It may be expected that the weighted compact nonlinear schemes are more efficient than CNS on vector machines.

For the convective flux calculations, the interpolations are usually approximated in the characteristic fields. Denotes as $\mathbf{l}^p$(row vector) and $\mathbf{r}^p$(column vector) the pth left and right eigenvectors of matrix $A = \partial E/\partial U$, considering the interpolation in cell $[x_{j-1/2}, x_{j+1/2}]$ for the pth characteristic variables $Q_{j,p}$,

$$Q_{j,p} = \mathbf{l}_n^p \cdot U_j, \tag{9}$$

where the subscript n is a function of the cell $[x_{j-1/2}, x_{j+1/2}]$. n is fixed as j for the interpolation of $\tilde{Q}_j(x)$ in the cell $[x_{j-1/2}, x_{j+1/2}]$. The general third-order interpolation of Q_j (the subscript p is omitted here) in $[x_{j-1/2}, x_{j+1/2}]$ can be written as

$$\tilde{Q}_j(x) = Q_j + (x - x_j) f_j + \frac{1}{2}(x - x_j)^2 s_j, \tag{10}$$

where f_j and s_j approximate first and second derivatives Q'_j and Q''_j, respectively. Assume

$$f_j = Q'_j + O(h^2), \quad s_j = Q''_j + O(h), \tag{11}$$

and we may get third-order cell-edge interpolated values,

$$\begin{aligned} \tilde{Q}_{Lj+1/2} &= \tilde{Q}_j\left(x_j + \frac{h}{2}\right) = Q_j + \frac{h}{2} f_j + \frac{1}{8}h^2 s_j, \\ \tilde{Q}_{Rj-1/2} &= \tilde{Q}_j\left(x_j - \frac{h}{2}\right) = Q_j - \frac{h}{2} f_j + \frac{1}{8}h^2 s_j. \end{aligned} \tag{12}$$

The subscripts L and R are introduced for upwind consideration.

In the region $[x_{j-2}, x_{j-1}, x_j, x_{j+1}, x_{j+2}]$, three kinds of f_j and s_j can be obtained at three different stencils, i.e.,

$$\begin{aligned} f_j^1 &= \frac{1}{2h}(Q_{j-2} - 4Q_{j-1} + 3Q_j), \\ f_j^2 &= \frac{1}{2h}(Q_{j+1} - Q_{j-1}), \\ f_j^3 &= \frac{1}{2h}(-3Q_j + 4Q_{j+1} - Q_{j+2}) \end{aligned} \tag{13}$$

and

$$\begin{aligned} s_j^1 &= \frac{1}{h^2}(Q_{j-2} - 2Q_{j-1} + Q_j), \\ s_j^2 &= \frac{1}{h^2}(Q_{j-1} - 2Q_j + Q_{j+1}), \\ s_j^3 &= \frac{1}{h^2}(Q_j - 2Q_{j+1} + Q_{j+2}). \end{aligned} \tag{14}$$

Note that Eqs. (13) and (14) satisfy conditions (11). When they are inserted into Eq. (12), the corresponding interpolations are $\tilde{Q}^1_{L(R)j\pm1/2}$, $\tilde{Q}^2_{L(R)j\pm1/2}$, and $\tilde{Q}^3_{L(R)j\pm1/2}$ respectively, which are third-order accurate. In order to get fifth-order accurate interpolations, we may combine these three values together with the weights ω_k,

$$\tilde{Q}^\omega_{Lj+1/2} = \sum_{k=1}^{3} \omega_{Lk} \tilde{Q}^k_{Lj+1/2}, \quad \tilde{Q}^\omega_{Rj-1/2} = \sum_{k=1}^{3} \omega_{Rk} \tilde{Q}^k_{Rj-1/2}, \tag{15}$$

and the requirements for $\omega_{L(R)k}$ are

$$\sum_{k=1}^{3} \omega_{Lk} = 1, \quad \sum_{k=1}^{3} \omega_{Rk} = 1. \tag{16}$$

On the other hand, in the region $[x_{j-2}, x_{j-1}, x_j, x_{j+1}, x_{j+2}]$, a fifth-order interpolation at cell-edge $x_{j\pm1/2}$ may be obtained as

$$\begin{aligned} \tilde{Q}^{\text{op}}_{j+1/2} &= Q_j + \frac{1}{128}(3Q_{j-2} - 20Q_{j-1} - 38Q_j + 60Q_{j+1} - 5Q_{j+2}) \\ \tilde{Q}^{\text{op}}_{j-1/2} &= Q_j - \frac{1}{128}(5Q_{j-2} - 60Q_{j-1} + 38Q_j + 20Q_{j+1} - 3Q_{j+2}) \end{aligned} \tag{17}$$

Thus, the optimal weights of $\omega_{L(R)k}$, i.e., $C_{L(R)k}$, can be obtained by the equivalents

$$\tilde{Q}^{\mathrm{op}}_{j+1/2} = \sum_{k=1}^{3} C_{Lk}\tilde{Q}^{k}_{Lj+1/2}, \quad \tilde{Q}^{\mathrm{op}}_{j-1/2} = \sum_{k=1}^{3} C_{Rk}\tilde{Q}^{k}_{Rj-1/2}, \tag{18}$$

and we get

$$C_{L1} = C_{R3} = \frac{1}{16}, \quad C_{L2} = C_{R2} = \frac{10}{16}, \quad C_{L3} = C_{R1} = \frac{5}{16}.$$

It is obvious that

$$\sum_{k=1}^{3} C_{Lk} = 1, \quad \sum_{k=1}^{3} C_{Rk} = 1. \tag{19}$$

By (15) and (18), the weighted interpolations (15) can be rewritten as

$$\begin{aligned} \tilde{Q}^{\omega}_{Lj+1/2} &= \tilde{Q}^{\mathrm{op}}_{Lj+1/2} + \sum_{k=1}^{3}(\omega_{Lk} - C_{Lk})\tilde{Q}^{k}_{Lj+1/2}, \\ \tilde{Q}^{\omega}_{Rj-1/2} &= \tilde{Q}^{\mathrm{op}}_{Rj-1/2} + \sum_{k=1}^{3}(\omega_{Rk} - C_{Rk})\tilde{Q}^{k}_{Rj-1/2}, \end{aligned} \tag{20}$$

and the last terms represent the high-order truncation errors. We may see this clearly by further writing these terms as follows by means of (16) and (19),

$$\begin{aligned} \sum_{k=1}^{3}(\omega_{Lk} - C_{Lk})\tilde{Q}^{k}_{Lj+1/2} &= \sum_{k=1}^{3}(\omega_{Lk} - C_{Lk})\big(\tilde{Q}^{k}_{Lj+1/2} - Q\big(x_{j+1/2}\big)\big), \\ \sum_{k=1}^{3}(\omega_{Rk} - C_{Rk})\tilde{Q}^{k}_{Rj-1/2} &= \sum_{k=1}^{3}(\omega_{Rk} - C_{Rk})\big(\tilde{Q}^{k}_{Rj-1/2} - Q\big(x_{j-1/2}\big)\big). \end{aligned} \tag{21}$$

With (21), we note that if

$$\omega_{Lk} = C_{Lk} + O(h^2), \quad \omega_{Rk} = C_{Rk} + O(h^2), \tag{22}$$

the weighted interpolations (15) or (20) are fifth-order accurate, i.e.,

$$\tilde{Q}^{\omega}_{Lj+1/2} = Q\big(x_{j+1/2}\big) + O(h^5), \quad \tilde{Q}^{\omega}_{Rj-1/2} = Q\big(x_{j-1/2}\big) + O(h^5).$$

The weights are defined by

$$\omega_{Lk} = \frac{\beta_{Lk}}{\sum_{m=1}^{3}\beta_{Lm}}, \quad \omega_{Rk} = \frac{\beta_{Rk}}{\sum_{m=1}^{3}\beta_{Rm}},$$

where

$$\beta_{Lk} = \frac{C_{Lk}}{(\epsilon + IS_k)^2}, \quad \beta_{Rk} = \frac{C_{Rk}}{(\epsilon + IS_k)^2}$$

$\epsilon = 10^{-6}$ is a small number to avoid the denominator becoming zero, and IS_k is a smooth measure. In this paper, we simply define the smooth measures IS_k as

$$IS_k = \big(hf^{k}_{j}\big)^2 + \big(h^2 s^{k}_{j}\big)^2.$$

It is obvious that in smooth regions

$$IS_k = (Q'h)^2(1 + O(h^2))$$

and the conditions (22) are satisfied. Thus, the interpolation values

$$Q^{\omega}_{Lj+1/2} = Q_j + \frac{h}{2} f^*_{Lj} + \frac{1}{8}h^2 s^*_{Lj}, \quad Q^{\omega}_{Rj-1/2} = Q_j - \frac{h}{2} f^*_{Rj} + \frac{1}{8}h^2 s^*_{Rj} \tag{23}$$

are fifth-order accurate in smooth regions, where

$$\begin{aligned} f^*_{Lj} &= \sum_{k=1}^{3} \omega_{Lk} f^k_j, \quad s^*_{Lj} = \sum_{k=1}^{3} \omega_{Lk} s^k_j, \\ f^*_{Rj} &= \sum_{k=1}^{3} \omega_{Rk} f^k_j, \quad s^*_{Rj} = \sum_{k=1}^{3} \omega_{Rk} s^k_j. \end{aligned}$$

Finally, the dependent variables at cell edges can be obtained as

$$\begin{aligned} \tilde{U}_{Lj+1/2} &= \sum_{p=1}^{3} \tilde{Q}^{\omega}_{Lj+1/2,p} \mathbf{r}^p_n, \\ \tilde{U}_{Rj-1/2} &= \sum_{p=1}^{3} \tilde{Q}^{\omega}_{Rj-1/2,p} \mathbf{r}^p_n. \end{aligned} \tag{24}$$

In practical calculations, the characteristic interpolations given above have high costs. In [11], a simple method was used to save computing time. Setting

$$\begin{aligned} a_j &= \left(\frac{4}{5}\delta^2_j \rho - \delta^2_{j-1}\rho\right)\left(\frac{5}{4}\delta^2_j \rho - \delta^2_{j-1}\rho\right), \\ b_j &= \left(\frac{4}{5}\delta^2_j \rho - \delta^2_{j+1}\rho\right)\left(\frac{5}{4}\delta^2_j \rho - \delta^2_{j+1}\rho\right), \end{aligned}$$

where ρ is the density and $\delta^2_j \rho = \rho_{j-1} - 2\rho_j + \rho_{j+1}$, if

$$\max(a_j, b_j) > \epsilon\rho, \tag{25}$$

the characteristic interpolations (10)–(24) are adopted ($\epsilon = 10^{-5}$). Otherwise, the grid point x_j is located in a smooth region, and the optimal interpolations (17) are used for the dependent variables U directly. It was found in our calculations that this technique is efficient, but the residuals can only converge to 10^{-6}–10^{-7}, though the solutions seem acceptable. Therefore, this technique is not recommanded for accurate calculations.

The Fourier Analysis of WCNS

In this section, we further discuss the dissipative and dispersive properties of WCNS by Fourier analysis. The scalar linear hyperbolic equation is considered here

$$\frac{\partial u}{\partial t} + c\frac{\partial u}{\partial x} = 0, \tag{26}$$

where $c > 0$ is a constant speed. The semi-discrete form of Eq. (26) can be written as

$$\frac{\partial u_j}{\partial t} + cu'_j = 0. \tag{27}$$

By differencing a periodic function,

$$u \equiv \exp(iwx), \tag{28}$$

we define the modified wave number $w^* = w^*_r + iw^*_i$ as

$$u' = iw^* \exp(iwx). \tag{29}$$

The accurate solutions of Eq. (27) with the initial condition (28) can be obtained by inserting $u(x, t) = A(t) \exp(iwx)$ into Eq. (27) to get

$$u_j = \exp(cw^*_i t) \exp\left[iw\left(x_j - c\frac{w^*_r}{w}t\right)\right]. \tag{30}$$

The cell-centered schemes (4) for the u'_j have the form

$$\kappa u'_{j-1} + u'_j + \kappa u'_{j+1} = \frac{a}{h}\left(\tilde{u}_{Lj+1/2} - \tilde{u}_{Lj-1/2}\right) + \frac{b}{h}\left(\tilde{u}_{Lj+3/2} - \tilde{u}_{Lj-3/2}\right). \tag{31}$$

Note that only $\tilde{u}_L$ need to be interpolated because $c > 0$. What we are most interested in is the solution on smooth regions. So the optimal interpolation

$$\tilde{u}_{j+1/2} = u_j + \frac{1}{128}(3u_{j-2} - 20u_{j-1} - 38u_j + 60u_{j+1} - 5u_{j+2}). \tag{32}$$

is used for analysis. Inserting Eqs. (28) and (29) into (32) and (31), we get the modified wave number function

$$w^*h = w^*(wh)h. \tag{33}$$

Figure 2 shows the real and imaginary parts of w^*h of WCNS compared with the explicit up wind biased fifth-order scheme (EUW5) and fourth-order Páde schemes. It may be noted that in terms of the modified wave numbers, the WCNS-5 scheme is a little superior to the EUW5 scheme which was successfully applied to the direct numerical simulation of turbulences, WCNS-4 and WCNS-E-4 have almost the same dispersive and dissipative features, and the WCNS schemes approach the fourth-order Páde scheme except that the dissipative errors are confined to intermediate and high wave numbers. Comparing Fig. 2 with Fig. 1, it is known that the interpolations of the variables at cell edges change the dispersive features of WCNS. It may be observed that $w^*_i h < 0$ for all cases in Fig. 2, which just corresponds to the dissipative property of the schemes. In Ref. [10], we gave a detailed discussion of this feature.

Boundary Schemes and Asymptotic Stability of WCNS

For high-order finite difference schemes development, it is important to derive boundary and near boundary schemes. As shown by Gustaffson [16], for a pth order interior scheme, the accuracy of boundary schemes can be $(p - 1)$th order accurate without reducing the

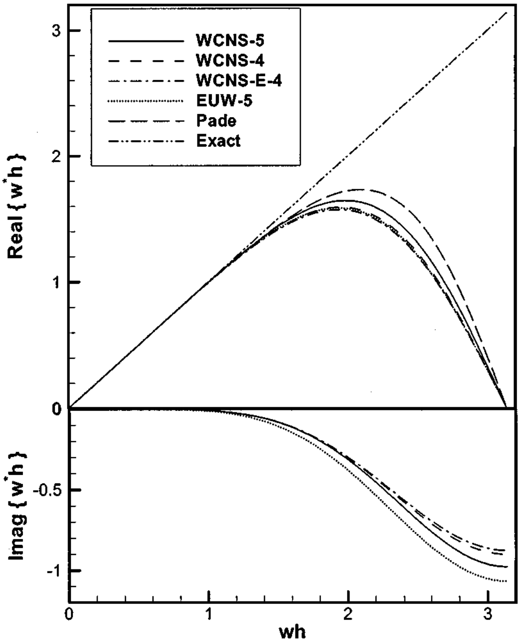

FIG. 2. The modified wave number of WCNS compared with fifth-order explicit upwind biased scheme and Pade scheme.

global accuracy of the interior scheme. For the fourth and fifth WCNS interior schemes, we derive the fourth-order boundary schemes

$$\begin{aligned} u_1' + \alpha_1 u_2' &= \frac{1}{h}\left(a_1\tilde{u}_{1/2} + b_1\tilde{u}_{3/2} + c_1\tilde{u}_{5/2} + d_1\tilde{u}_{7/2} + e_1\tilde{u}_{9/2}\right),\\ u_N' + \alpha_1 u_{N-1}' &= -\frac{1}{h}\left(a_1\tilde{u}_{N+1/2} + b_1\tilde{u}_{N-1/2} + c_1\tilde{u}_{N-3/2} + d_1\tilde{u}_{N-5/2} + e_1\tilde{u}_{N-7/2}\right), \end{aligned} \tag{34}$$

where

$$\begin{gathered} a_1 = \frac{1}{24}(\alpha_1 - 22), \quad b_1 = \frac{1}{24}(17 - 27\alpha_1), \quad c_1 = \frac{1}{24}(9 + 27\alpha_1),\\ d_1 = -\frac{1}{24}(5 + \alpha_1), \quad e_1 = \frac{1}{24}. \end{gathered}$$

As $\alpha = -71/31$, this is fifth-order accurate. For boundary and near boundary interpolation, the explicit fourth-order interpolants are derived:

$$\begin{aligned} \tilde{u}_{1/2} &= \frac{1}{16}(5u_0 + 15u_1 - 5u_2 + u_3),\\ \tilde{u}_{3/2} &= \frac{1}{16}(-u_0 + 9u_1 + 9u_2 - u_3),\\ \tilde{u}_{N-1/2} &= \frac{1}{16}(5u_N + 15u_{N-1} - 5u_{N-2} + u_{N-3}),\\ \tilde{u}_{N+1/2} &= \frac{1}{16}(35u_N - 35uN_{N-1} + 21u_{N-2} - 5u_{N-3}). \end{aligned} \tag{35}$$

Substituting (31), (32), (34), and (35) into (27) leads to

$$\mathbf{A}\frac{d\mathbf{u}}{dt} = \frac{c}{h}\mathbf{BCu} + \mathbf{g}(t),$$

where $\mathbf{u} = (u_1, u_2, \ldots, u_N)^T$, $\mathbf{g}(t)$ corresponds to initial and boundary conditions (without losing generality, we set $\mathbf{g}(t) = 0$ in the following analysis), and

$$\mathbf{A} = \begin{pmatrix} 1 & \alpha_1 & & & & & \\ \kappa & 1 & \kappa & & & & \\ & \cdot & \cdot & \cdot & & & \\ & & \kappa & 1 & \kappa & & \\ & & & \cdot & \cdot & \cdot & \\ & & & & \kappa & 1 & \kappa \\ & & & & & \alpha_1 & 1 \end{pmatrix}_{N\times N},$$

$$\mathbf{B} = -\begin{pmatrix} a_1\text{‘} & b_1 & c_1 & d_1 & e_1 & & & \\ -b & -a & a & b & & & & \\ & \cdot & \cdot & \cdot & \cdot & & & \\ & & -b & -a & a & b & & \\ & & & \cdot & \cdot & \cdot & \cdot & \\ & & & & -b & -a & a & b \\ & & & -e_1 & -d_1 & -c_1 & -b_1 & -a_1 \end{pmatrix}_{N\times(N+1)}$$

$$\mathbf{C} = \begin{pmatrix} \frac{15}{16} & -\frac{5}{16} & \frac{1}{16} & & & & & & \\ \frac{9}{16} & \frac{9}{16} & -\frac{1}{16} & & & & & & \\ -\frac{20}{128} & \frac{90}{128} & \frac{60}{128} & -\frac{5}{128} & & & & & \\ \frac{3}{128} & -\frac{20}{128} & \frac{90}{128} & \frac{60}{128} & -\frac{5}{128} & & & & \\ & \cdot & \cdot & \cdot & \cdot & \cdot & & & \\ & & \frac{3}{128} & -\frac{20}{128} & \frac{90}{128} & \frac{60}{128} & -\frac{5}{128} & & \\ & & & \cdot & \cdot & \cdot & \cdot & \cdot & \\ & & & & & \frac{1}{16} & -\frac{5}{16} & \frac{15}{16} & \frac{5}{16} \\ & & & & & -\frac{5}{16} & \frac{21}{16} & -\frac{35}{16} & \frac{35}{16} \end{pmatrix}_{(N+1)\times N}$$

As discussed in [1], the asymptotic stability condition for the semi-discrete equation is that all eigenvalues of the matrix $\mathbf{R} = \mathbf{A}^{-1}\mathbf{BC}$ have no positive parts.

Figure 3 shows the eigenvalue spectra for the WCNS-E-4, WCNS-4, and WCNS-5 on the uniform grid. It can be seen that these schemes are all asymptotically stable. Further calculations show that the parameter α_1 in the boundary scheme (34) has little effect on the asymptotic stability.

For practical calculations, especially for viscous flow simulations, the stretching grids are necessary. In order to investigate the effect of grid stretching, we transform Eq. (26) from the stretching physical space x to the uniform computational domain ξ by

$$x(\xi) = \frac{A(\beta + 2\alpha) + 2\alpha - \beta}{(2\alpha + 1)(1 + A)}, \quad A = \left(\frac{\beta + 1}{\beta - 1}\right)^{(1-\xi-\alpha)/(\alpha-1)}, \tag{36}$$

where $\alpha = 0.5$ and $\beta = 1.01015$ are constants [17]. Based on this transformation, the matrix $\mathbf{R}$ is changed as $\tilde{\mathbf{R}} = \mathbf{D}^{-1}\mathbf{R}$ and $\mathbf{D} = \mathrm{diag}(x_{\xi 1}, x_{\xi 2}, \cdots\cdots, x_{\xi N}\}$. The eigenvalue spectra

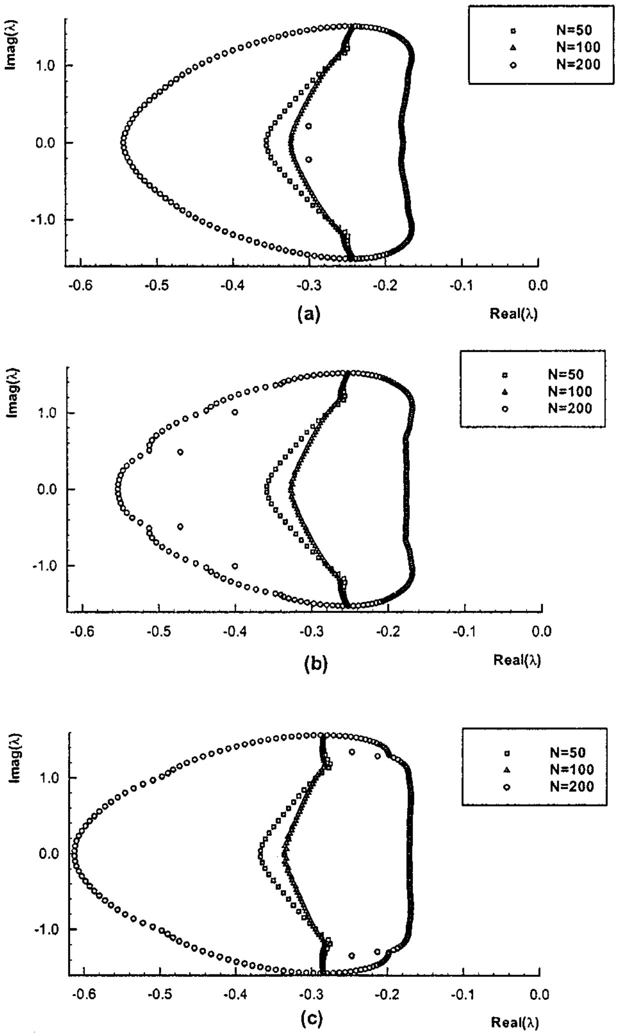

FIG. 3. The eigenvalue spectra on uniform grids: (a) WCNS-E-4, (b) WCNS-4, and (c) WCNS-5.

of WCNS on this stretching grid is showed in Fig. 4. We know from the figure that WCNS become unstable as the grid number equal to 50, a very strong stretched grid. With the increasing of the grid number, the relative stretching of the grid reduces and the schemes become stable. Therefore, in practical simulations we should pay attention to the strong stretching grids which may have destabilizing effect on WCNS. On the other hand, for the viscous flow simulations, the physical viscosity has the stabilizing effect, such that the overall schemes may be stable.

In practical calculations, the last two interpolants in Eq. (35) may be replaced by

$$
\begin{aligned}
\tilde{u}_{N-1/2} &= \frac{1}{16}(-u_{N+1} + 9u_N + 9u_{N-1} - u_{N-2}), \\
\tilde{u}_{N+1/2} &= \frac{1}{16}(5u_{N+1} + 15u_N - 5u_{N-1} + u_{N-2}).
\end{aligned}
\tag{37}
$$

The boundary and near boundary schemes (34), (35), and (37) can be used in the convective

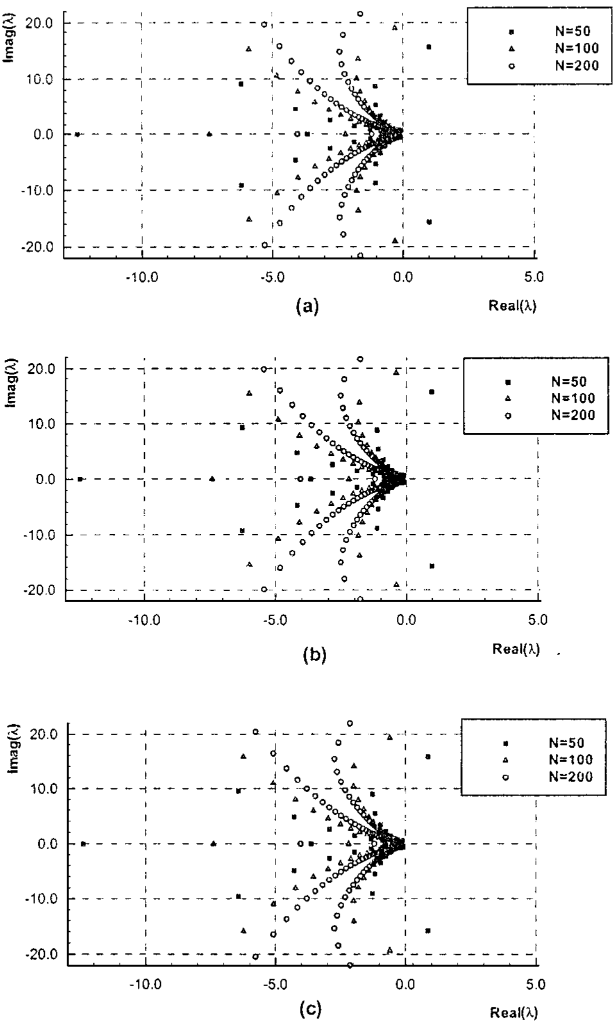

FIG. 4. The eigenvalues spectra on stretching grids: (a) WCNS-E-4, (b) WCNS-4, and (c) WCNS-5.

flux of Euler and Navier–Stokes equations directly, with u' replaced by E', $\tilde{u}$ by $\tilde{U}$, and u by U, respectively.

Upwind Flux Splitting Schemes

One advantage of WCNS is that the interpolation procedure is independent of the numerical flux calculations. As the cell-edge values have been interpolated, there are various ways to construct the numerical flux. We have used Roe's flux difference scheme,

$$\tilde{E}^{\mathrm{Roe}}_{j+1/2} = \frac{1}{2}\left[E\left(\tilde{U}_{Rj+1/2}\right) + E\left(\tilde{U}_{Lj+1/2}\right) - |\tilde{A}|\left(\tilde{U}_{Rj+1/2} - \tilde{U}_{Lj+1/2}\right)\right], \tag{38}$$

in the CNS [8, 9]. In fact, the flux vector splitting schemes,

$$\tilde{E}^{\mathrm{FV}}_{j+1/2} = E^{-}\left(\tilde{U}_{Rj+1/2}\right) + E^{+}\left(\tilde{U}_{Lj+1/2}\right), \tag{39}$$

can also be used. Here, $E^{\pm}$ may be obtained by Steger and Warming's or Van Leer's splitting or other flux vector splitting methods. Furthermore, the flux themselves can be used to interpolate the cell-edge values by (9)–(24) and get

$$\begin{aligned}\tilde{E}^F_{j+1/2} &= \tilde{E}^+_{j+1/2} + \tilde{E}^-_{j+1/2};\\ \tilde{E}^+_{j+1/2} &= E^+_j + \frac{h}{2}F^{+*}_j + \frac{1}{8}h^2 S^{+*}_j,\\ \tilde{E}^-_{j+1/2} &= E^-_{j+1} - \frac{h}{2}F^{-*}_{j+1} + \frac{1}{8}h^2 S^{-*}_{j+1},\end{aligned} \tag{40}$$

where $F^{\pm} = \partial E^{\pm}/\partial x$ and $S^{\pm} = \partial^2 E^{\pm}/\partial x^2$. In this paper, we compared Eqs. (38) and (39) in the Euler equation calculations.

Discretizations of Viscous Flux for Navier–Stokes Equations

In the above section, we only discussed the convective flux discretization. For the Navier–Stokes equations calculations, the cell-centered compact scheme (4) can also be applied to viscous flux, i.e.,

$$\kappa E'_{vj-1} + E'_{vj} + \kappa E'_{vj+1} = \frac{a}{h}\left(\tilde{E}_{vj+1/2} - \tilde{E}_{vj-1/2}\right) + \frac{b}{h}\left(\tilde{E}_{vj+3/2} - \tilde{E}_{vj-3/2}\right). \tag{41}$$

The viscous flux $\tilde{E}_{vj+1/2}$ at cell edges contains first-order derivatives of the dependent variables as well as the dependent variables themselves. We first use the high-order central type compact schemes to calculate these values, and then substitute them into Eq. (41) to obtain the derivatives of the viscous flux. In Appendix, we give the detailed schemes required for the viscous flux calculation at the cell edges.

Time Discretization

We treat Eq. (3) as an ordinary differential equation,

$$\frac{\partial U}{\partial t} = R(U), \tag{42}$$

and employ the third-order TVD Runge–Kutta method [14] for the time integration:

$$\begin{aligned}U^{(1)} &= U^n + \Delta t R(U^n)\\ U^{(2)} &= \frac{3}{4}U^n + \frac{1}{4}U^{(1)} + \frac{1}{4}\Delta t R\left(U^{(1)}\right)\\ U^{n+1} &= \frac{1}{3}U^n + \frac{2}{3}U^{(2)} + \frac{2}{3}\Delta t R\left(U^{(2)}\right).\end{aligned} \tag{43}$$

A fourth-order Runge–Kutta scheme is

$$\begin{aligned}U^{(1)} &= U^n + \frac{1}{2}\Delta t R(U^n)\\ U^{(2)} &= U^n + \frac{1}{2}\Delta t R\left(U^{(1)}\right)\\ U^{(3)} &= U^n + \Delta t R\left(U^{(2)}\right)\\ U^{n+1} &= \frac{1}{3}\left(-U^n + U^{(1)} + 2U^{(2)} + U^{(3)}\right) + \frac{1}{6}\Delta t R\left(U^{(3)}\right).\end{aligned} \tag{44}$$

It is not TVD type. In this paper, only Eq. (43) is used in the numerical tests.

3. NUMERICAL TESTS

In this section, we test the behaviors of the WCNS for several examples. The tests contain two groups. One is the Euler equation solutions, which are selected to show the ability of WCNS to resolve discontinuities. The another is the Navier–Stokes solutions which show the accuracy of WCNS in smooth regions, especially for the boundary layer simulations. The Roe flux difference scheme is used in one-dimensional cases.

EXAMPLE 1. The one-dimensional Riemann problem for the Euler equations of gas dynamics is solved with the initial conditions

$$(\rho_L, u_L, p_L) = (1, 0, 1), \quad (\rho_R, u_R, p_R) = (0.125, 0, 0.1). \tag{45}$$

In the calculation, we used the characteristic interpolations with 100 grid points, CFL $= 0.2$, and 200 time steps. The calculated density results are given in Fig. 5. Three WCNS(-S) give almost the same results (the suffix "-S" means the sharpening technique being used). The sharpening technique with $\sigma = 12$ can steepen the contact discontinuity at 3–4 grid points; here σ is a sharpening parameter. In [11], the details of the contact discontinuity sharpening technique can be found. Compared with the results calculated by WENO schemes [13], our resolution of the corner of rarefaction waves (discontinuities in derivatives) are improved.

EXAMPLE 2. This is the same equations as in Example 1 with the initial conditions

$$U^0(x) = \begin{cases} U_L, & 0 \le x < 0.1 \\ U_M, & 0.1 \le x < 0.9 \\ U_R, & 0.9 \le x < 1, \end{cases} \tag{46}$$

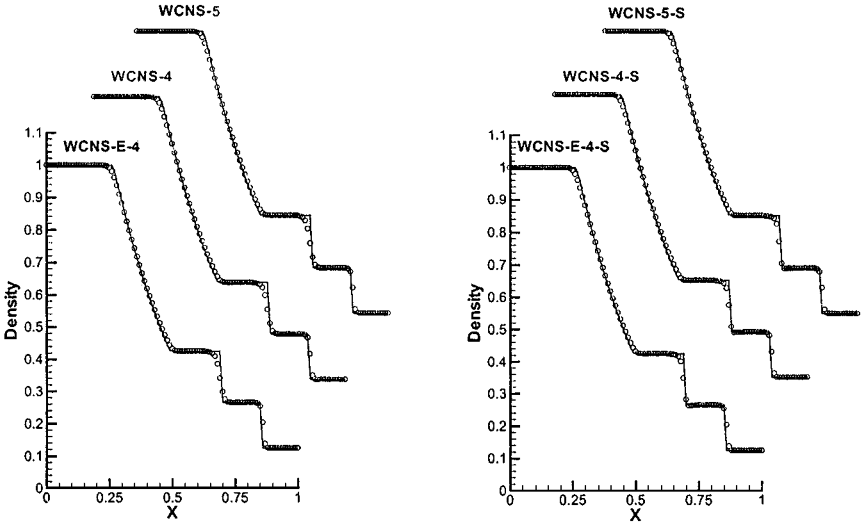

FIG. 5. The density distributions of shock tube flow with 100 grid calculations by WCNS.

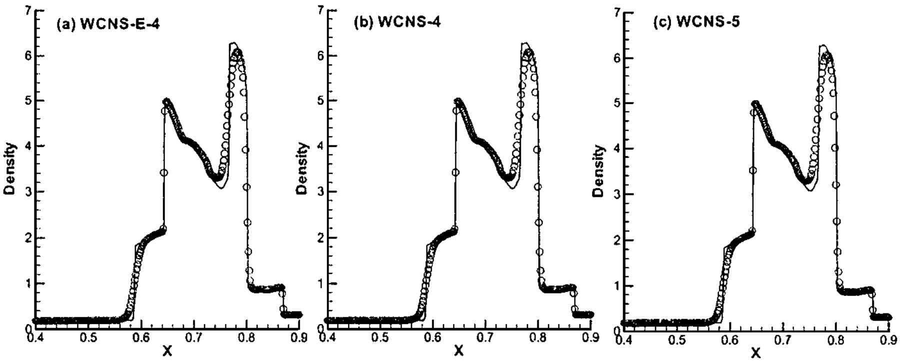

FIG. 6. The density distributions of a blast wave at $T = 0.038$ with 600 grids calculated by WCNS without contact sharpening.

where

$$\rho_L = \rho_M = \rho_R = 1, \quad u_L = u_M = u_R = 0, \quad p_L = 10^3, \quad p_M = 10^{-2}, \quad p_R = 10^2.$$

The boundaries at $x = 0$ and $x = 1$ are solid walls with reflecting boundary conditions. At the final time $t = 0.038$, the flow field has three contact discontinuities. The middle one, which is generated by the two shocks interacting with each other, is very difficult to resolve. Figure 6 shows the results without contact discontinuity sharpening with CFL $= 0.6$, 600 grid points. It should be pointed out that in our previous calculations, Figs. 4 and 5 in [11], there were small unphysical oscillations near the left shock. The oscillations were caused by Roe's flux splitting method. It is known that Roe's scheme may violate the entropy condition when the eigenvalues at the Roe-averaged state vanish. In the present calculations, we used another entropy fixing technique [18] in Roe's scheme and solved this problem. In fact, the flux vector splitting scheme (39) can also suppress the oscillation. Figure 7 shows the results calculated by WCNS-5-S with $\sigma = 12$. The solid lines are the results of the same methods with 1000 grid points ($\sigma = 12$). It can be seen that the discontinuities, including the

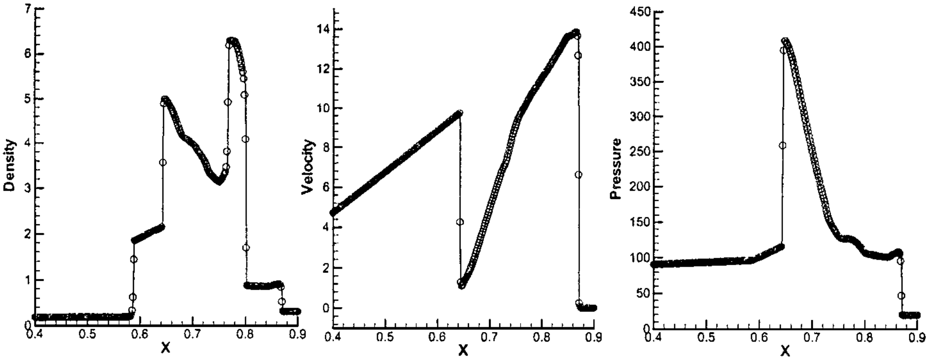

FIG. 7. The blast wave results at $T = 0.038$ with 600 grids calculated by WCNS-5-S.

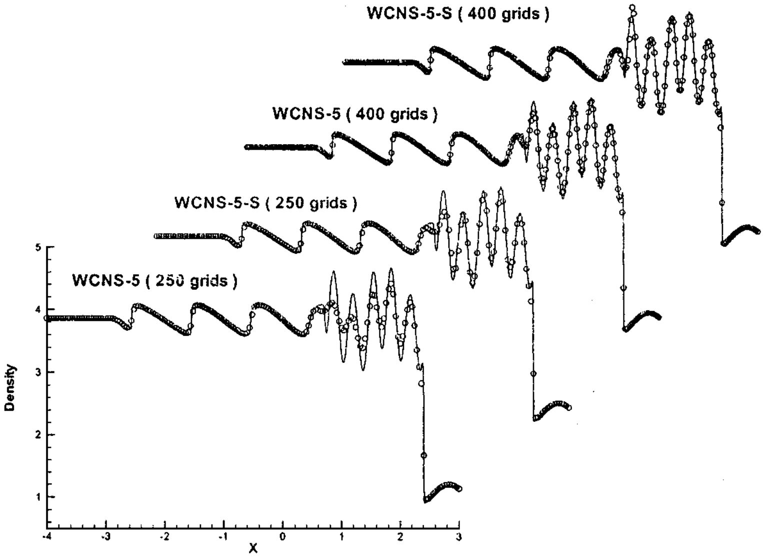

FIG. 8. The density distributions of "shock/turbulence" interactions calculated by WCNS-5.

middle contact discontinuity, are resolved well. Compared with fifth-order WENO results [13] with Yang's artificial compressing technique, the middle contact discontinuity of our results is captured more sharply.

EXAMPLE 3. The third example is a model problem for the shock/turbulence interaction. It originates from the following initial conditions:

$$(\rho, u, p) = \begin{cases} (3.857143, 2.629369, 10.33333) & x < 4, \\ (1 + 0.2 \sin 5x, 0, 1) & x \geq 4. \end{cases} \tag{47}$$

Figure 8 shows the density results calculated by WCNS-5-(S) with 250 and 400 grid points and $\sigma = 7$. The main fine structure was resolved on 250 grid points by the sharpening technique. The solid lines in this figure were calculated by CNS [8, 9] with 1600 grid points. It can be regarded as the exact solution.

EXAMPLE 4. The fourth example is two-dimensional wind tunnel flow with a step at Mach 3. Woodward and Colella [19] investigated this flow carefully. The wind tunnel is 1 length unit wide and 3 length units long. The step is 0.2 length units high and located 0.6 length unit from the left-hand end of the tunnel. The problem is initialized by a right-moving Mach 3 flow. Reflective boundary conditions are imposed at wind tunnel walls and step surface. In-flow and out-flow boundary conditions are applied at the left-hand and right-hand sides, respectively. For the treatment of the corner of the step, the method suggested in [19] is adopted.

In the calculations, two grids were used. The first one is the medium grid with 121 × 41 grid points and the fine grid contains 241 × 81 grid meshes. CFL = 0.6 is used for all the calculations. Figures 9 and 10 show the density contours calculated by WCNS-E-4, WCNS-4, and WCNS-5 on these two grids. The Steger–Warmings flux vector splitting method was used here. The results show that WCNS perform well for this example. They have good

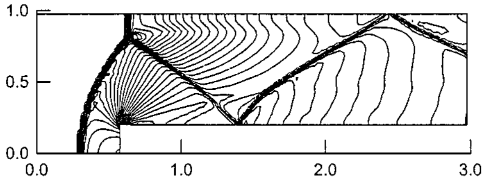

(a) WCNS-E-4 with Steger-Warming flux splitting.

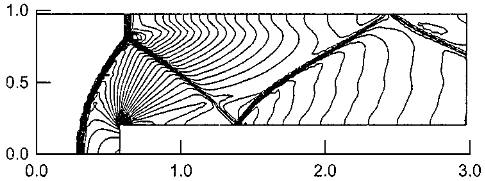

(b) WCNS-4 with Steger-Warming flux splitting.

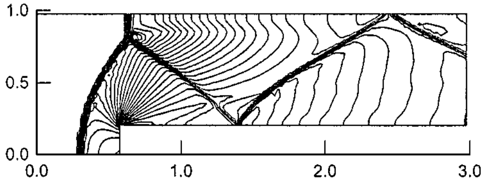

(c) WCNS-5 with Steger-Waring flux splitting.

FIG. 9. Density contrours of flow past a step on a medium grid, 121 × 41, at $t = 4$: (a) WCNS-E-4, (b) WCNS-4, and (c) WCNS-5.

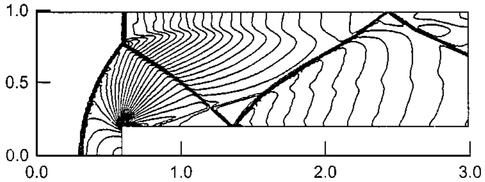

(a) WCNS-E-4 with Steger-Warming flux splitting.

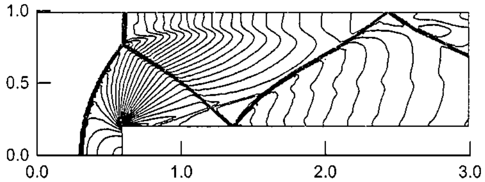

(b) WCNS-4 with Steger-Warning flux splitting.

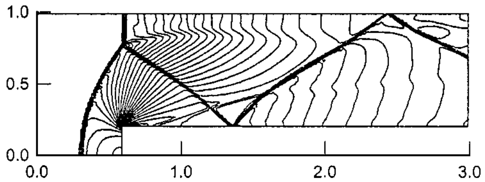

(c) WCNS-5 with Steger-Waring flux splitting.

FIG. 10. Density contours of flow past a step on a fine grid, 241 × 81, at $t = 4$: (a) WCNS-E-4, (b) WCNS-4, and (c) WCNS-5.

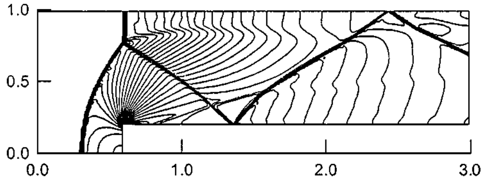

(a) WCNS-5 with Steger-Warming flux splitting.

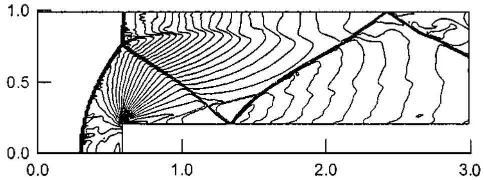

(b) WCNS-5 with Roe flux difference splitting.

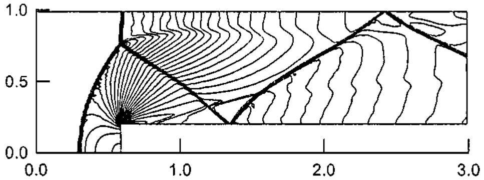

(c) WCNS-5 with Van Leer flux splitting.

FIG. 11. Density contours of flow past a step on a fine grid, 241 × 81, at $t = 4$ with: (a) WCNS-5 Steger–Warming flux splitting, (b) WCNS-5 Roe flux difference splitting, and (c) WCNS-5 Van Leer flux splitting.

resolutions for the shock and contact discontinuity. The results on the fine grid are almost the same as that of the PPM scheme [19]. Furthermore, there are almost no differences between WCNS-4 and WCNS-5, which confirms that the weighted interpolation dominates the accuracy of WCNS.

Figure 11 shows the results calculated by WCNS-5 on a fine grid with different flux splitting methods. We know from this figure that Steger–Warming and Van Leer flux vector splitting gave more smooth solutions than Roe flux difference scheme for this problem.

EXAMPLE 5. The last example is steady hypersonic viscous flow around a circular cylinder. We select this problem because there is a spectral solution [20] that can be used for the comparison, especially for the heat transfer on the body surface. The flow conditions are $M_\infty = 5.73$, $\mathrm{Re} = 2050$, $T^*_\infty = 39.6698$ K, $T^*_w = 210.2$ K, $\gamma = 1.4$, $\mathrm{Pr} = 0.77$, and the cylinder radius $r^* = 0.0061468$ m.

Figure 12 gives the results by WCNS-5 with Steger–Warming flux splitting on a 61 × 61 grid. It can be seen that the bow shock is captured well and the pressure coefficient and heat transfer in Fig. 13 compare well with the spectral solution. In order to investigate the grid convergence, we repeated the calculations on two other grids 31 × 31 and 15 × 21. The pressure coefficient and heat transfer on the body surface shown in Fig. 14 compare well with the spectral solution on the three grids, and Fig. 15 shows the convergent history. All the residuals on these three grids converge to machine zero.

For the comparison of the WCNS with the high resolution TVD type or MUSCL schemes, we calculated this flow by MUSCL scheme on 15 × 21 grid. Figure 16 shows the surface pressure coefficient and heat transfer. Though the MUSCL scheme can give a good pressure coefficient, the heat transfer compares poorly with the WCNS and spectral solutions. This confirms the high-order accuracy of WCNS.

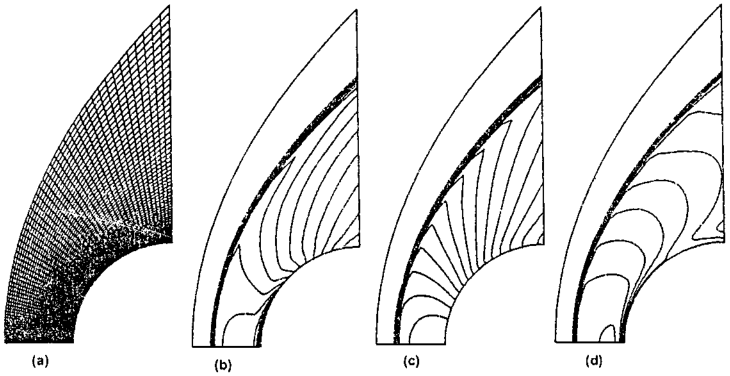

FIG. 12. Contours calculated by WCNS-5 with 61 × 61 grids: (a) grid, (b) density, (c) pressure, and (d) temperature.

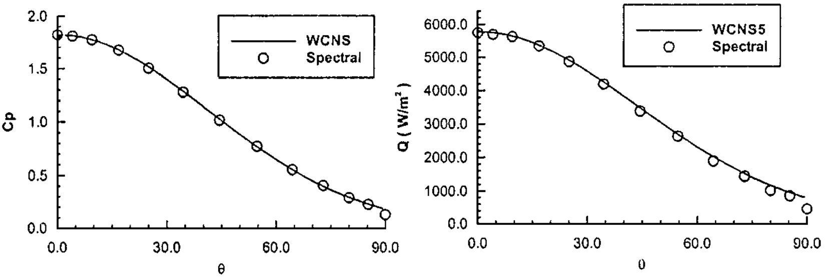

FIG. 13. The surface pressure (C_p) and heat transfer (Q) distribution on grid 61 × 61 compared with the spectral method.

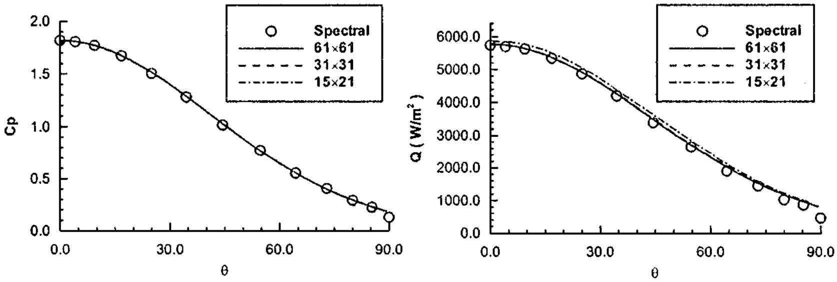

FIG. 14. The surface pressure (C_p) and heat transfer (Q) distribution on various grids compared with the spectral method.

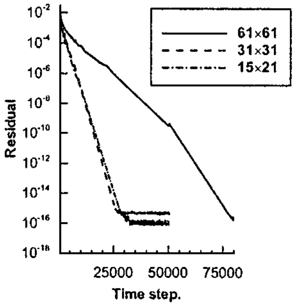

FIG. 15. The convergent history on various grids.

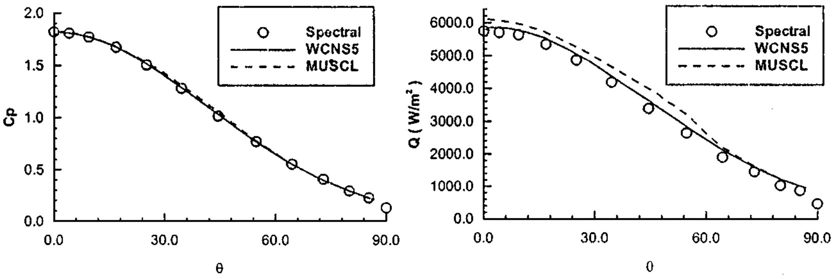

FIG. 16. The surface pressure (C_p) and heat transfer (Q) distribution on grid 15×21 compared with MUSCL scheme.

4. CONCLUDING REMARKS

Weighted compact nonlinear schemes (WCNS) are developed in this paper. By Fourier analysis, the dispersive and dissipative features of WCNS in smooth regions were discussed, which showed that the interpolations of variables at cell edges dominate the accuracy of the schemes and WCNS have almost same accuracy as the fifth-order upwind biased explicit linear scheme in smooth regions. Asymptotic stability analysis shows that the boundary and near boundary schemes developed in this paper, as well as the interior schemes, are asymptotically stable on the uniform grid. On the stretching grids, the schemes are also asymptotically stable, as the stretching is not very strong. One of the advantages of WCNS is that the dependent variable interpolation is independent of the flux splitting schemes, so that we have the freedom to select various flux splitting schemes according to various flows. One- and two-dimensional Euler equation calculations showed that WCNS can capture discontinuities robustly. Hypersonic steady viscous flow simulations showed that WCNS can give results comparable to the spectral method solution and the residuals can converge to machine zero. Furthermore, the viscous numerical results confirmed that the WCNS are more accurate than the MUSCL scheme, as expected.

In this paper, we only showed the performance of WCNS for one- and two-dimensional calculations. Further research is to apply them to three-dimensional Navier–Stokes equations for the DNS of hypersonic stability problems, large eddy simulations (LES) of complex turbulent flows to show the accuracy of WCNS for the resolution of the fine structures.

APPENDIX

For the viscous term calculations, the following derivative schemes and interpolation schemes are needed.

(1) The compact first-order derivatives at cell edges:

$$
\begin{aligned}
u'_{1/2} + \alpha_1 u'_{3/2} &= \frac{1}{h}(a_1 u_0 + b_1 u_1 + c_1 u_2 + d_1 u_3 + e_1 u_4),\\
\kappa u'_{j-1/2} + u'_{j+1/2} + \kappa u'_{j+3/2} &= \frac{a}{h}(u_{j+1} - u_j) + \frac{b}{h}(u_{j+2} - u_{j-1}), \qquad (A1)\\
u'_{N+1/2} + \alpha_1 u'_{N-1/2} &= -\frac{1}{h}(a_1 u_{N+1} + b_1 u_N + c_1 u_{N-1} + d_1 u_{N-2} + e_1 u_{N-3}).
\end{aligned}
$$

The parameters in these schemes are the same as in (31) and (34).

(2) The compact first-order derivatives at grid nodes:

$$\begin{gathered}
u_1' + 3u_2' = \frac{1}{6h}(-17u_1 + 9u_2 + 9u_3 - u_4),\\
\frac{1}{4}u_1' + u_2' + \frac{1}{4}u_3' = \frac{3}{4h}(u_3 - u_1),\\
\frac{1}{3}u_{j-1}' + u_j' + \frac{1}{3}u_{j+1}' = \frac{1}{36h}(u_{j+2} - u_{j-2}) + \frac{7}{9h}(u_{j+1} - u_{j-1}),\\
\frac{1}{4}u_{N-2}' + u_{N-1}' + \frac{1}{4}u_N' = \frac{3}{4h}(u_N - u_{N-2}),\\
u_N' + 3u_{N-1}' = -\frac{1}{6h}(-17u_N + 9u_{N-1} + 9u_{N-2} - u_{N-3}).
\end{gathered} \tag{A2}$$

(3) The compact interpolation at cell edges:

$$\alpha u_{j-1/2} + u_{j+1/2} + \alpha u_{j+3/2} = \frac{10\alpha + 9}{16}(u_{j+1} + u_j) + \frac{6\alpha - 1}{16}(u_{j+2} + u_{j-1}). \tag{A3}$$

As $\alpha = \frac{3}{10}$ the interpolant is sixth-order accurate. Two sets of boundary schemes can be derived:

$$\begin{aligned}
u_{1/2} &= \frac{1}{16}(35u_1 - 35u_2 + 21u_3 - 5u_4),\\
u_{3/2} &= \frac{1}{16}(5u_1 + 15u_2 - 5u_3 + u_4),\\
u_{N-1/2} &= \frac{1}{16}(5u_N + 15u_{N-1} - 5u_{N-2} + u_{N-3}),\\
u_{N+1/2} &= \frac{1}{16}(35u_N + 35u_{N-1} + 21u_{N-2} - 5u_{N-3}),
\end{aligned} \tag{A3.1}$$

and

$$\begin{aligned}
u_{1/2} &= \frac{1}{16}(5u_0 + 15u_1 - 5u_2 + u_3),\\
u_{N+1/2} &= \frac{1}{16}(5u_{N+1} + 15u_N - 5u_{N-1} + u_{N-2}),
\end{aligned} \tag{A3.2}$$

(4) The compact interpolation at grid nodes:

$$\begin{aligned}
u_1 &= \frac{1}{16}\left(5u_{1/2} + 15u_{3/2} - 5u_{5/2} + u_{7/2}\right),\\
\alpha u_{j-1} + u_j + \alpha u_{j+1} &= \frac{10\alpha + 9}{16} + \left(u_{j+1/2} + u_{j-1/2}\right) + \frac{6\alpha - 1}{16}\left(u_{j+3/2} + u_{j-3/2}\right),\\
u_N &= \frac{1}{16}\left(5u_{N+1/2} + 15u_{N-1/2} - 5u_{N-3/2} + u_{N-5/2}\right).
\end{aligned} \tag{A4}$$

Also, as $\alpha = \frac{3}{10}$ the interior interpolant is sixth-order accurate.

ACKNOWLEDGMENTS

This work was supported by the project of Basic Research on Frontier Problems in Fluid and Aerodynamics in China and the China National Natural Science Foundation. The first author acknowledges associate professor M. L. Mao discussing the problem with him.

REFERENCES

1. S. K. Lele, Compact finite difference schemes with spectral-like resolution, *J. Comput. Phys.* **103**, 16 (1992).
2. R. V. Wilson, A. Q. Demuren, and M. H. Carpenter, High-order compact schemes for numerical simulations of incompressible flows, ICASE Report 98-13 ICASE, Langley Research Center (1998).
3. L. M. Leslie and R. J. Purser, Three-dimensional mass-conserving semi-Lagrangian scheme employing forward tajectories, *Mon. Weather Rev.* **123**, 2551 (1995).
4. V. A. Garanzha and Konshin, Numerical algorithms for viscous incompressible fluid flows based on the high-order conservative compact schemes, *Comput. Math. Math. Phys.* **8**, 1321 (1999).
5. D. Gaitonde and J. S. Shang, Optimized compact-difference-based finite-volume schemes for linear wave phenomena, *J. Comput. Phys.* **138**, 617 (1997).
6. M. H. Kobayashi, On a class of Pade finite volume methods, *J. Comput. Phys.* **156**, 137 (1999).
7. B. Cockburn and C. W. Shu, Nonlinearly stable compact schemes for shock calculations, *SIAM J. Numer. Anal.* **31**, 607 (1994).
8. X. G. Deng and H. Maekawa, Compact high-order accurate nonlinear schemes, *J. Comput. Phys.* **130**, 77 (1997).
9. X. G. Deng and H. Maekawa, An uniform fourth-order nonlinear compact schemes for discontinuities capturing, in *AIAA paper 96-1974, 27th AIAA Fluid Dynamics Meeting* (New Orleans, LA, AIAA, 1996).
10. X. G. Deng, H. Maekawa, and Q. Shen, A class of high-order dissipative compact schemes, in *AIAA paper 96-1972, 27th AIAA Fluid Dynamics Meeting* (New Orleans, LA, AIAA, 1996).
11. X. G. Deng and M. L. Mao, Weighted compact high-order nonlinear schemes for the Euler equations, AIAA Paper 97-1941, presented of the 13th AIAA Computational Fluid Dynamic Conference (Snowmass).
12. X. D. Liu, S. Osher, and T. Chan, Weighted essentially non-oscillatory schemes, *J. Comput. Phys.* **115**, 200 (1994).
13. G. S. Jiang and C. W. Shu, Efficient implementation of weighted ENO schemes, ICASE Report, No. 95-73, 1995; also NASA CR 198228 (1995).
14. C. W. Shu and S. Osher, Efficient implementation of essentially non-oscillatory shock-capturing schemes II, *J. Comput. Phys.* **83**, 32 (1989).
15. H. T. Huynh, Accurate upwind methods for the Euler equations, *SIAM J. Numer. Anal.* **32**(5), 1565 (1995).
16. B. Gustaffson, The convergence rate for difference approximations to mixed initial boundary value problems, *Math. Comput.* **49**(130), 396 (1975).
17. G. O. Roberts, Computational meshes for the boundary problems, in *Proc. Second International Conf. Numerical Methods Fluid Dyn.*, Lecture Notes in Physics (Springer–Verlag, New York, 1971), p. 171.
18. D. Gaitonde and J. S. Shang, Accuracy of flux-split algorithms in high-speed viscous flows, *AIAA J.* **31**, 1215 (1993).
19. P. Woodward and P. Collela, The numerical simulation of two-dimensional fluid flow with strong shocks, *J. Comput. Phys.* **54**, 115 (1984).
20. D. A. Kopriva, Spectral solution of the viscous blunt-body problem, *AIAA J.* **31**, 1235 (1993).